https://doi.org/10.1016/j.wear.2017.11.008

Surface damage mechanism of monocrystalline silicon during single point diamond grinding

Quanli Zhang[1*], Yucan Fu[1], Honghua Su[1], Qingliang Zhao[2] and Suet To[3]

[1] College of Mechanical and Electrical Engineering, Nanjing University of Aeronautics and Astronautics, Nanjing 210016, China

[2] Centre for Precision Engineering, School of Mechatronics Engineering, Harbin Institute of Technology, Harbin, 150001, China

[3] State Key Laboratory of Ultra-precision Machining Technology, The Hong Kong Polytechnic University, Hong Kong

*Corresponding Author / E-mail: zhangql606@163.com, TEL: +025-84895857, FAX: +025-84895857

Abstract

Surface damage mechanism of single crystalline Si (100) under single point diamond grinding was investigated in the present study. The result, for the first time, showed that the ductile and brittle material removal appeared at different grinding positions of the diamond wheel due to the varied kinematics of the diamond grits in the cylindrical face and end face. Under the dynamic pressure of the diamond grits, amorphization and the transformation to high pressure phases (Si-III and Si-XI) of Si occurred, which were identified by both XRD and Raman spectroscopy. In addition, surface oxidation and chemical reaction between the Si, O, C and N atoms was analyzed by the XPS, and the new products of Si_3N_4 and graphite oxide (GO) are firstly proposed to be the surface damage of Si and the tool wear mechanism during the ultra-precision machining process.

Keywords: Single point diamond grinding; Monocrystalline Si; Tribochemistry; Phase transformation

1. Introduction

As a famous semiconductor material, monocrystalline Si is now widely used in the fields of electronics, infrared optical devices and photovoltaic technologies. However, for its high brittleness and the chemical activity with carbon, there is still great difficulty to machine them to obtain the damage-free surface by the ultra-precision machining technology. For instance, single point diamond turning (SPDT) has been applied to obtain the nanometric surface on Si [1], but the chemical reaction between Si and C always results in the serious tool wear [2, 3], which makes the diamond turning process more costly. To overcome the problem, ultra-precision grinding process was applied to fabricate the Si devices [4]. However, surface and subsurface damage can be introduced by the dynamic pressure of the diamond grits, such as the phase transformations [5, 6], surface fracture [7, 8], residual stress [9] and edge chipping [4]. Actually, the efficiency and the service life of the devices are closely related to the surface damage degree induced by the grinding process. Such kinds of defects are actually intolerable for Si wafers used for the intergrated circuits (ICs) and photovoltaics. For example, the residual stress and surface fracture can result in an immediate decrease of the module efficiency and stability [10, 11].

The damage mechanism of monocrystalline Si is closely related to the material removal mode. Ductile material removal has been widely investigated to reduce the

surface fracture during ultra-precision machining of brittle materials [12]. In addition, phase transformation of Si also contributed to the surface fracture under a rapid loading/unloading condition [13, 14]. Specifically, it has been reported that the transformation of crystalline Si-I to metallic Si-II (β-Sn structure) occurred during the loading stage, and the Si-II phase further turned to be r8 structure (Si-XII) or bc8 structure (Si-III) during the unloading process [13]. A volume change appeared for the different densities of the polymorph phases of Si, which led to the generation of abnormal load-displacement curves (elbow or pop-out) during nano-indentation [13-15]. In the previous studies, the phase transformation of Si during the diamond scratching, diamond turning and abrasive machining has also been identified and investigated [16-19]. However, the effects of phase transformation on the nanometric surface characteristics have been rarely discussed. Moreover, the high temperature generated by the friction and fracture can lead to the chemical reactions between the Si atoms and the diamond tool and oxygen [20, 21].

For ultra-precision grinding technology, another encountered problem is the size limitation of the parts caused by the dimension of the diamond wheel and the grinding methodology. For instance, it is difficult to machine the aspherical or spherical parts with a higher aspect ratio by conventional method. As a new grinding process, wheel normal grinding which is typical type of single point diamond grinding process was developed to overcome the size limitation of the parts [22-24]. In the wheel normal grinding process, a sharp edge on the diamond wheel is necessary to prevent interference between the diamond wheel and the designed surface [25, 26], and the

sharp edge of wheel is kept to be normal to the machined surface all the time. To ensure that the sharp edge of the diamond wheel participated in the material removal and surface generation process, the diamond wheel was moved with gradient tilted angle by integrating *B* axis rotation to adjust the relative position of diamond wheel and workpiece surface. Brinksmeier et al [27] and Tohme [22] both pointed out that this method can prevent the transfer of wheel error to the machined spherical surface. However, the utilization of the novel grinding process in the fabrication of Si devices has not been reported. During the single point diamond grinding process of Si, the number of the diamond grits decreased, and the surface characteristics of the ground Si should also be changed.

In the present work, single point diamond grinding of single crystalline Si wafer is performed to get a further understanding of the surface damage mechanism. To reveal the damage mechanism of Si, the scanning electron microscope (SEM), X ray photoelectron spectroscopy (XPS), Raman spectroscopy, energy dispersive spectroscopy (EDS) and X ray diffraction (XRD) are utilized to examine the machined Si surface, in terms of the nanometric surface characteristics, oxidation, chemical reaction and the amorphization.

2. Experiments

Commercially available monocrystalline silicon wafer N-Si(100) (Top Vendor Science & Technology Co., Ltd. China) with the size of 15×15×0.5 mm was used as the workpiece, and it is fixed to a round clip made of Al. Single point diamond grinding (SPDG) of the Si(100) wafer was conducted on an ultra-precision grinding machine

(Moore Nanotech 450UPL, USA), equipped with two linear slides (X and Z axis) and one rotational axis (B axis), as illustrated in Fig. 1. Commercially available Clairsol 350 (Haltermann Carless USA Inc.) was used as coolant, which is composed of parafinic hydrocarbon from petroleum distillates, principally decane (hydrotreated light, kerosene-unspecified 60-100%). To obtain a smooth machined surface and achieve the ductile material removal, a 2000# resin bonded diamond wheel (Diagrind, Inc., USA) was utilized. The average diameter of the diamond grits can be obtained to be around 3.7 μm by the following empirical equation [28],

$$d_g = 28.9 \cdot g^{-1.18} \tag{1}$$

where g is the grain size and d_g is the mean grain diameter. Before it was applied for the diamond grinding process, the cylindrical wheel was firstly dressed by a green SiC stick to obtain a sharp edge of 90 ° angle. Single point diamond grinding was then conducted with the sharp edge perpendicular to the machined surface which was controlled by the B axis. The detail grinding parameters are listed in Table 1.

The surface morphology of the machined Si(100) sample was characterized by a scanning electron microscope (SEM, JEOL Model JSM-6490), equipped with an energy disperse spectroscopy (EDS). The surface topography was examined by a white light interferometer (WLI, ZYGO Lamda Nexview) and an atomic force microscope (AFM, Park's XE-70). In addition, the phase structure of the Si(100) after grinding was studied by X ray diffraction (XRD, Rigaku SmartLab) with the CuK_α radiation (45 kV, 200 mA), X ray photoelectron spectroscopy (XPS, ESCALAB 250Xi) and Raman spectroscopy (Raman, Horiba Xplora system) with the laser wavelength of 532 nm.

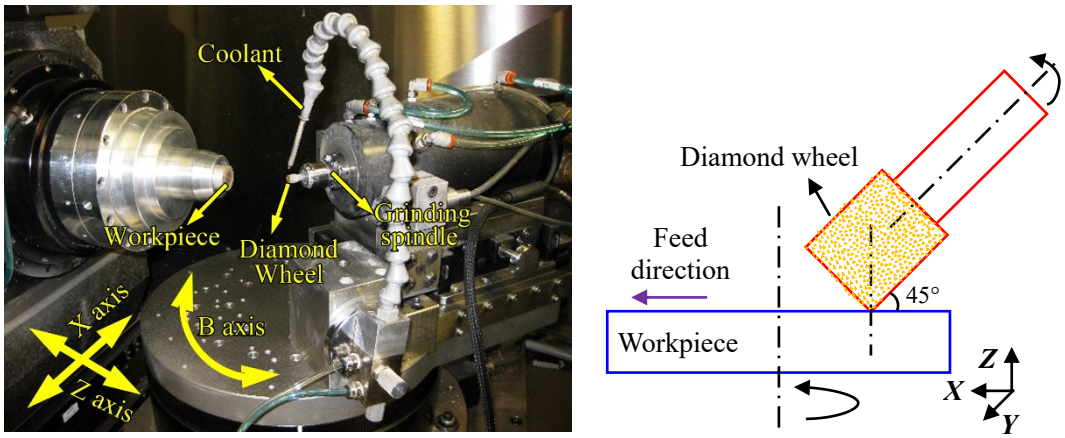

Fig.1 Schematic of the grinding setup and grinding methodology

Table 1 Detail grinding parameters

2000# diamond wheel	diam. 8 mm, resin bonded
Wheel RPM n_s (rpm)	50,000
Workpiece RPM n_w (rpm)	120
Feed rate f (mm/min)	0.5
Depth of grinding a_e (μm/pass)	0.5
Coolant	CLAIRSOL 350 (MQL)
Workpiece size (mm)	15×15×0.5

3. Results

The surface topography of the machined Si(100) is shown in Fig. 2. It can be found that the surface roughness can reach R_a=14.56 nm, R_q=16.60 nm and R_t=83.15 nm, as shown in Fig. 2(a). The micro-grooves caused by the wheel feed can be clearly seen. Fig. 2(b) shows the AFM image of the ground surface, and more fine scratching stripes generated by the diamond grits appeared in the micro-grooves, which are regarded as the indication for the ductile material removal. In addition, surface burs appeared on the machined surface, as shown in Fig. 2(b).

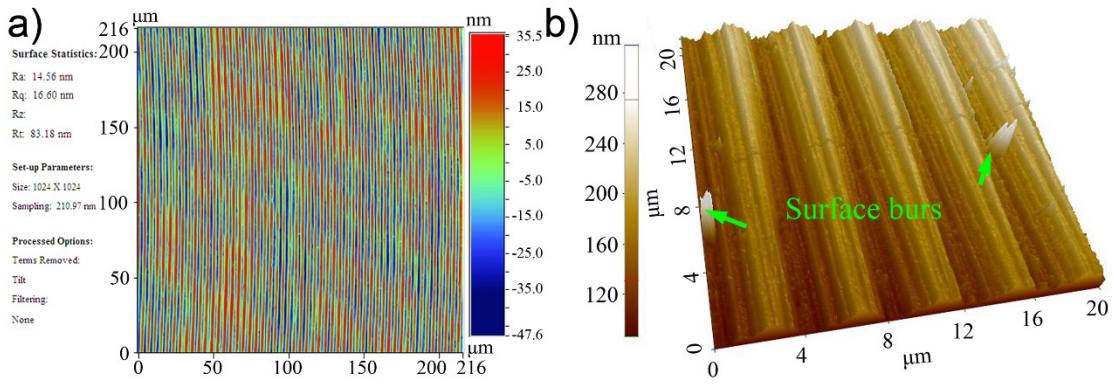

Fig. 2 (a) Surface topography, and (b) AFM image of the machined single crystalline Si

The surface morphology of the machined Si(100), as shown in Fig. 3(a), clearly indicates that the ground surface is covered by the brittle fractured regions and ductile smooth regions along the grinding direction. The ductile material removal was mainly produced by the diamond grits distributed in the sharp edge of the wheel, but the brittle fracture appeared at the peak positions of the cross-sectional profile. In addition, the intermittent break of the ground surface resulted in the formation of micro-pits of varied sizes. Interestingly, it can be seen that the color for the machined surface also varied at different points, which might be attributed to the formation of the varied allotrope phases of Si.

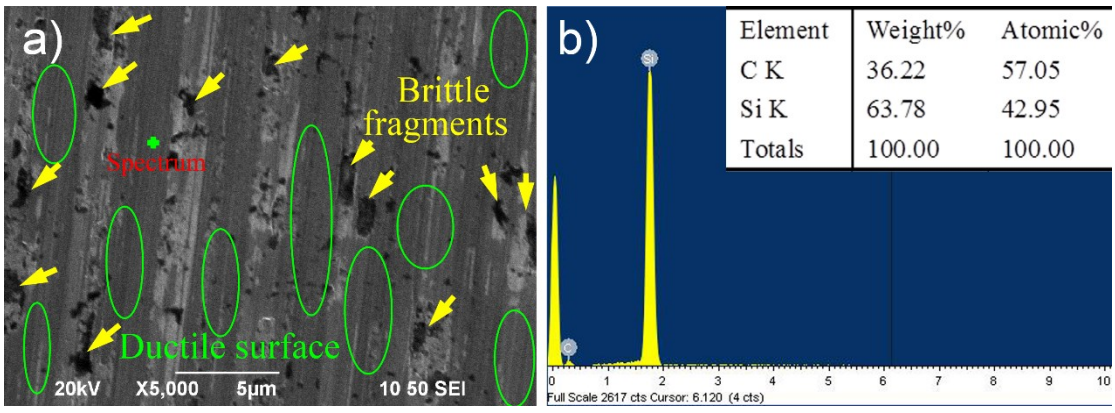

Fig. 3 SEM image and EDS result of the machined single crystalline Si surface

The EDS result, as shown in Fig. 3(b), indicates that a high ratio of C atoms remained on the machined Si(100) surface where the ductile material removal occurred. Under the dynamic scratching effects, the temperature in the grinding zone rose rapidly due to the friction effects, so the chemical reaction between the Si atoms and C atoms is supposed to be induced to form SiC, as indicated by the XRD result shown in Fig. 4. In addition, the abrasive wear of the diamond grits resulted in the adhesion of diamond materials on the machined surface. The broad diffraction peak at 2θ=68.5 ° appeared due to the amorphization of the crystalline Si.

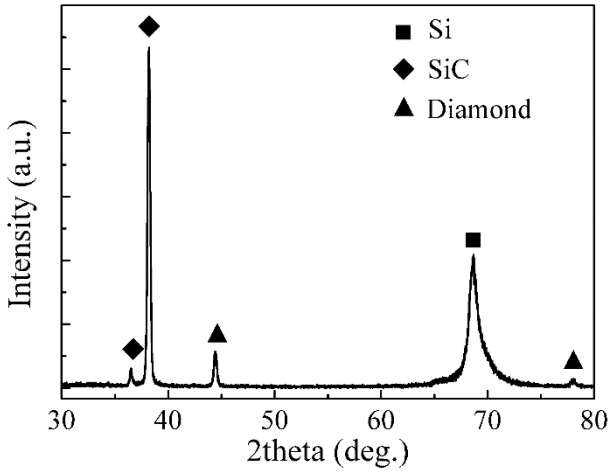

Fig. 4 X ray diffraction spectra of the machined Si(100) surface

To get a further insight into the chemical reaction during the grinding process, the XPS results of the machined surface are shown in Fig. 5. It is found from the full XPS spectra that C1s, N1s and O1s peaks can be clearly detected, as shown in Fig. 5(a). The full spectrum shows that there is a great amount of O element on the machined Si surface. The appearance of O is firstly attributed to the oxidation of Si, as illustrated in Fig. 5(b). The oxidation products of Si contain not only SiO_2 but also SiO. The peak information of Si_3N_4 can be obtained due to the chemical reaction between the Si atoms

and N_2. The formation of SiC is also verified by the results of the C peak separation, and the C atoms from diamond can be detected, as shown in Fig. 5(c). In addition, the C=O and C-O bonds formed due to the oxidation of C atoms, which indicates the appearance of graphite oxide (GO). The XPS peak of the O1s can be separated into C=O, SiO, SiO_2 and -OH peaks, as shown in Fig. 5(d). The result further confirms the oxidation of Si and the diamond grits during the grinding process.

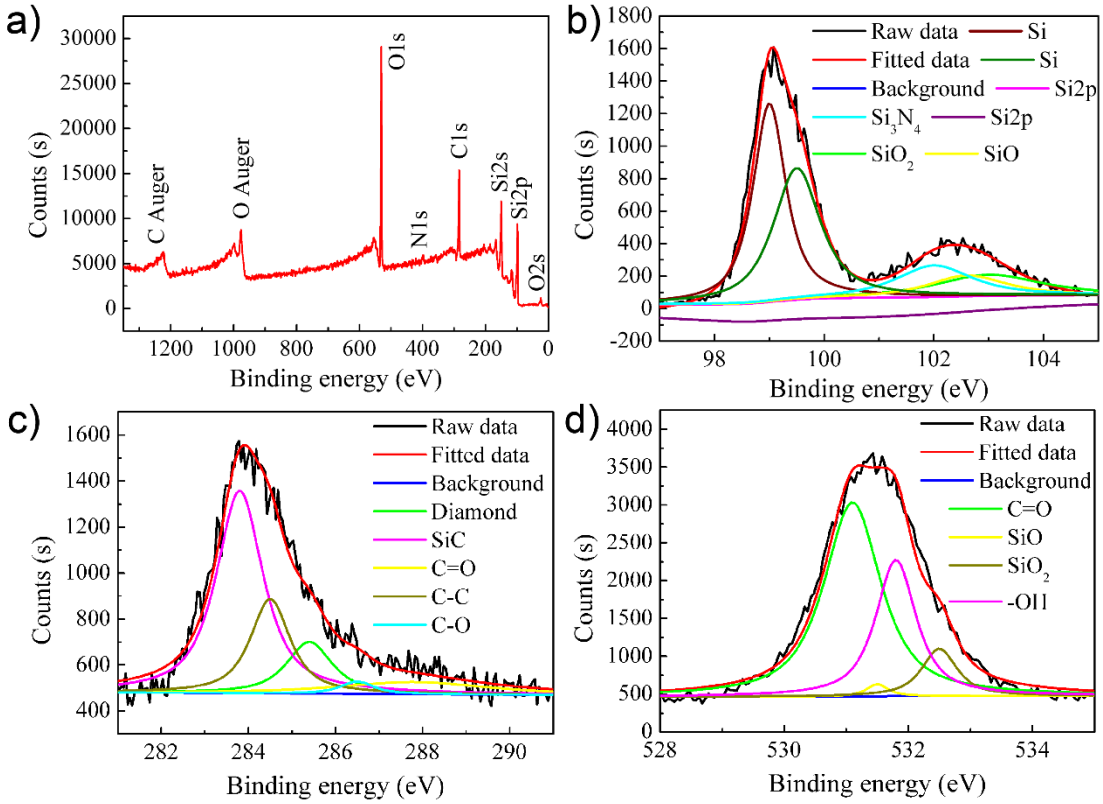

Fig. 5 XPS results of the machined single crystalline Si surface: a) full XPS spectrum; b) Si2p peak separation; c) C1s peak separation; d) O1s peak separation

Fig. 6 shows the Raman spectra of the polished Si surface and the ground Si surface. Compared with the original surface, as shown in Fig. 6(a), the Raman spectra of the machined Si surface further shows that the amorphization of Si was induced under the dynamic pressure of the diamond grits, where an asymmetry background

occurs around 470 cm^{-1} and the peak intensity at 520 cm^{-1} decreases, as shown in Fig. 6(b) and (c). Moreover, the phase transformation of the different allotropes of Si were induced at varied points of the machined surface. Specifically, the Si-I structure turns to be amorphous structure at Point 1, while the Si-XII and Si-III structure formed except the amorphous phase at point 2.

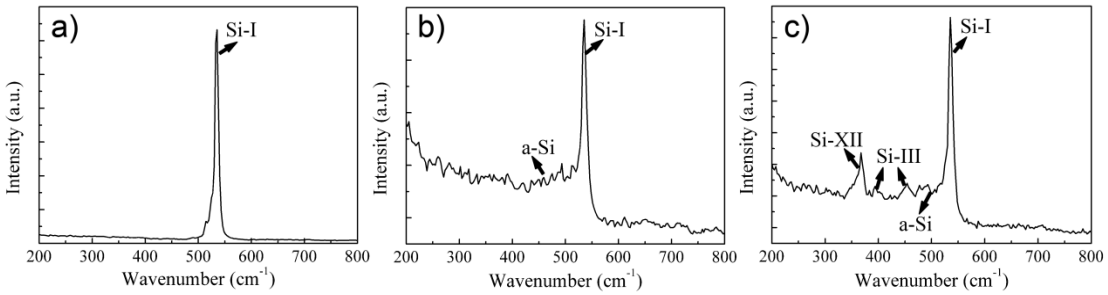

Fig. 6 Raman spectra of the polished Si wafer and the machined Si surface at different points: a) the polished Si surface; b) point 1 on the machined Si surface; c) point 2 on the machined Si surface

4. Discussion

For the machining of hard and brittle materials, the critical depth of cut is proposed by Bifano et al as follows [12],

$$d_c = 0.15 \cdot \left(\frac{E}{H}\right) \cdot \left(\frac{K_c}{H}\right)^2 \tag{2}$$

where d_c is the critical depth of cut, E is the elastic modulus, H is the hardness, and K_c is the fracture toughness of the machined material. By comparing the relative value of d_c and the maximum undeformed chip thickness h_m, the material removal mechanism can be obtained [29], where h_m could be calculated by Eq. (3) [30],

$$h_m = \left[\frac{4}{Cr}\left(\frac{v_w}{v_s}\right)\left(\frac{a_e}{d_e}\right)^{1/2}\right]^{1/2} \tag{3}$$

where v_s is the wheel speed, v_w is the workpiece speed, a_e is the grinding depth, d_e is the equivalent diameter of the wheel, C is the grit number per unit area in wheel, and r is the chip width-to-thickness ratio.

The critical cutting depth (d_c) of Si was calculated to be about 60 nm by Bifano et al based on Eq. (2) in Ref. [12]. Based on the previous study [31], the value of the grit number per unit area in wheel (C) and the chip width-to-thickness ratio (r) is chosen to be 55 and 90 for the used 2000# diamond wheel. Then, the maximum undeform chip thickness (h_m) can be obtained based on the parameters in Table 1. Fig. 7 shows the maximum undeform chip thickness of single crystalline Si according to Eq. (3). It can be easily seen that the value of h_m drops gradually with decreasing radial distance from the workpiece center due to the varied workpiece speed (v_w), as shown in Fig. 7(a). The condition for brittle material removal can be met when h_m is bigger than d_c (~60 nm). Even so, it should be noted that the undeform chip thickness for the different diamond grits also changed due to the random distribution in the wheel. The protrusion heights of the diamond grits distributed randomly, and some of the diamond grits with smaller protrusion heights contributed to the ductile materials removal. So both the ductile and brittle material removal can be achieved by different diamond grits, even though h_m is greater than d_c.

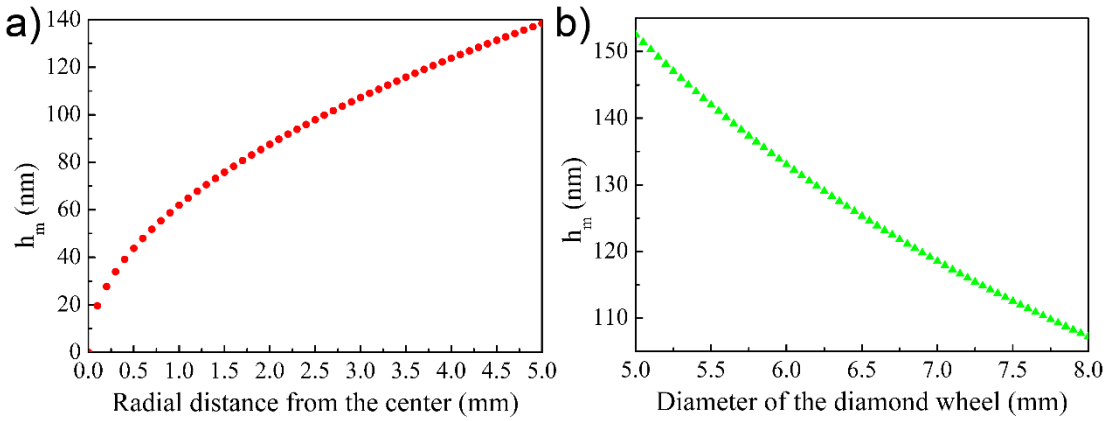

Fig. 7 The calculated maximum undeform chip thickness (h_m): a) the dependence on the radial distance from the workpiece center, b) the dependence on the diameter of the wheel

If the diamond wheel wear is not taken into consideration, the generation of the cross-sectional profile for the single point diamond grinding process (also referred as quick point grinding in [32] or wheel normal grinding in [22]) is illustrated in Fig. 8. Based on the analysis of the grinding kinematics, it can be found that the material is mainly removed by the diamond grits in the cylindrical surface of the diamond wheel, and the generated surfaces for the grinding grooves are named sides *B* in Fig. 8(a). The surface generation for sides A is different from sides B, where the diamond grits in the end face is responsible for the surface formation of sides A, as shown in Fig. 8(a). The scratching and squeezing effects led to the surface fracture for sides A. In addition, for the points at a smaller radial distance in A, both the cutting velocity and the equivalent rotation diameter of the diamond grits decreases compared with the diamond grit in the cylindrical surface. So the maximum undeformed chip thickness h_m become greater with decreasing diameter of the end face, as shown in Fig. 7(b), which promotes the brittle material removal. Therefore, the different material removal mechanism resulted

in the varied nanometric characteristics in the same grinding groove, as shown in Fig. 8(b).

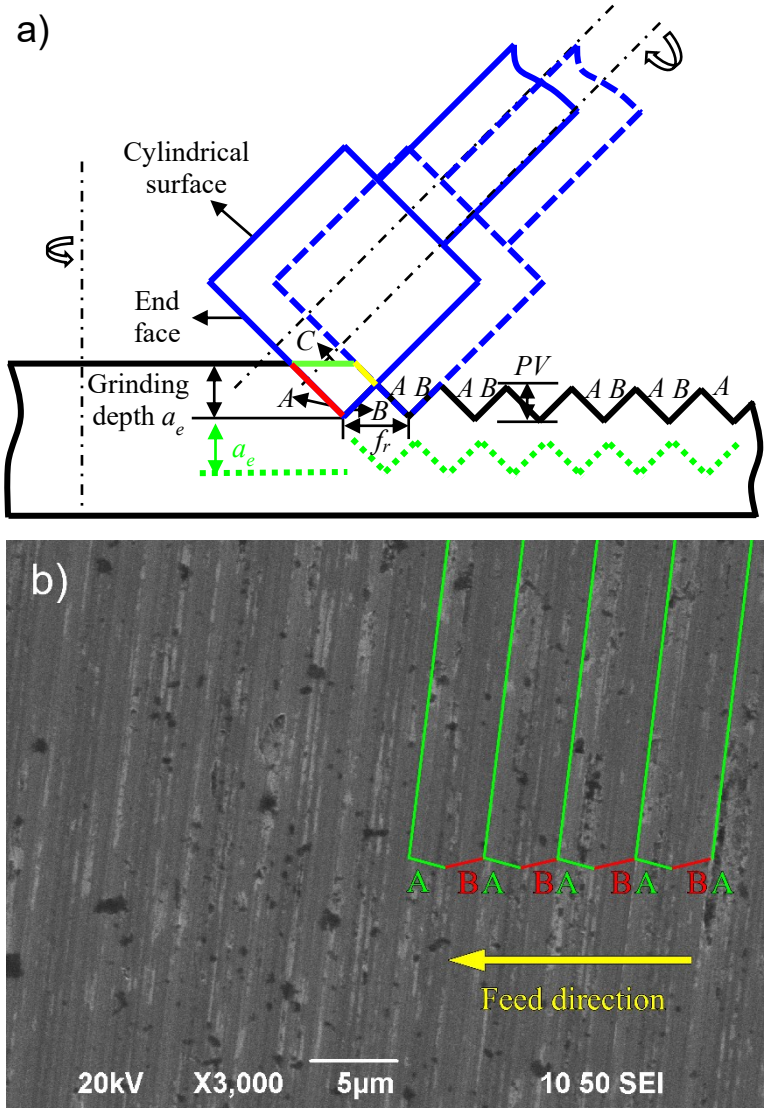

Fig. 8 (a) Illustration of the cross-sectional profile generated by single point diamond grinding; (b) SEM image of the grinding surface to illustrate the difference between sides A and sides B

For the micro-machining process by single point diamond grinding, the rapid wear of the sharp wheel edge would also affect the surface characteristics [23, 24]. The surface topography and cross-sectional profile of the diamond wheel after grinding is shown in Fig. 9(a) and (b). It can be easily seen that the 90° sharp edge obtained by the

diamond nib dressing experienced rapid wear during the grinding process, and it is referred to be the macro wheel wear which bears obvious impact on the form accuracy of the machined surface. Comparing the surface morphology of the diamond grits after dressing and grinding, as shown in Fig. 9(c) and (d), it is found that the abrasive wear and grooving wear appeared for the diamond grits. The surface of the diamond grits participated in the material removal becomes smooth and the flattening appeared compared with the grits after dressing. Even though the flattened surface might also prompt the ductile material removal during the machining of brittle materials in fine grinding [33], the heat generation and thermal loads rose in the grinding zone due to the increasing friction effects [34], and it has been reported that the thermal effects can lead to the melting of Si during the nanoscratching test [17]. Therefore, re-dressing of the diamond wheel is of great necessity during the grinding process.

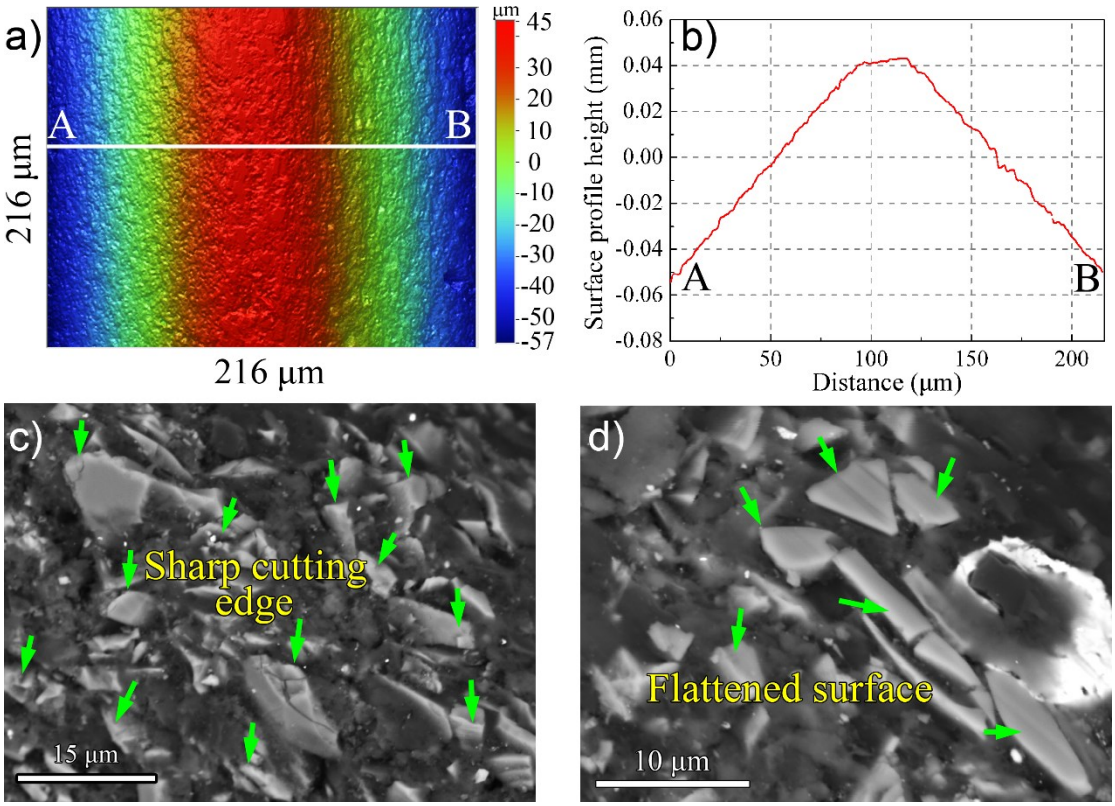

Fig. 9 (a) Surface topography and (b) cross-sectional profile of the diamond wheel after grinding; (c) SEM image of the diamond wheel after dressing; (d) SEM image of the diamond wheel after grinding

To get an insight into the temperature in the grinding zone, we try to analyze it by the Finite Element Modelling (FEM) method. The rake and clearance angle of the diamond grit used for simulation is 26.5°. Then, a simplified method based on D-P (Drucker-Prager) model can be built to analyze the grinding temperature, where the diamond grit is rotated to cut the workpiece material analogous to the raster-milling process [15], as shown in Fig. 10(a). Generally, multi-passes grinding are needed to obtain the final surface, and the generated surface of the current pass (indicated by the green dotted line) is actually related to the serrated surface (indicated by the black line) obtained by the previous grinding pass, as shown in Fig. 8(a). It can also be found that the diamond grits in the sharp edge of the wheel actually owns the maximum cutting depth. Taken the specific kinematic of the inclined axis grinding and the remained material of the serrated cross-section into consideration, the maximum cutting depth can be simply expressed as follows,

$$a_{e\,max} = \sqrt{2}a_e + PV \tag{4}$$

where a_{emax} is the maximum cutting depth of the diamond grit in the sharp edge, a_e is the grinding depth, and PV is the peak to valley value which can be measured by the white light interferometer(R_t). So the maximum cutting depth is chosen to be 0.75 μm based on the calculated a_{emax} (~790 nm), and the cutting parameters and the material parameters are listed in Table 1 and Table 2, respectively.

Table 2 Mechanical properties of Si(100) material

Elastic modulus E (MPa)	193000
Density ρ (ton/mm^3)	2.3×10^{9}
Possion's ratio	0.28
Fracture toughness K_{IC} (MPa m$^{1/2}$)	0.9
Yield stress (MPa)	7000
Angle of friction (°)	18
Dilation angle (°)	5
Flow stress ratio	0.9
Friction coefficient between Chip and Tool	0.2

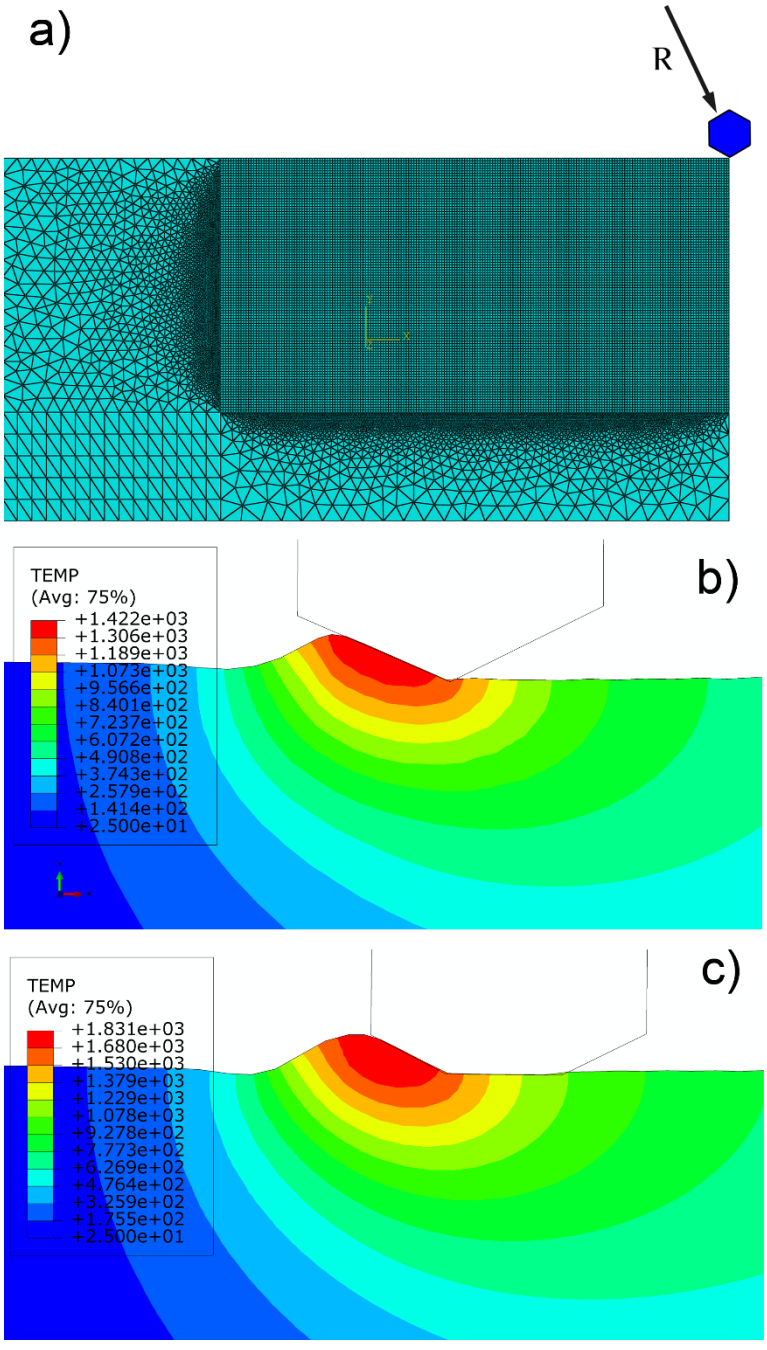

Fig. 10 The temperature distribution in the cutting zone simulated by the ABAQUS software: a) The built model, b) before wear, c) after wear

As shown in Fig. 10(b), the maximum temperature in the cutting zone can reach above 1400 ℃. The surface morphology of the diamond grits after grinding indicates that the flattening of the diamond grits resulted in the loss of the sharp cutting edge, and it leads to the further growth of the temperature in the cutting zone, as shown in Fig. 10(c).

Generally, the production of SiC matarials is always conducted at the temperature higher than 1400 ℃ [36], and the chemical reaction between solid Si and solid C can take place at around 800 ℃ [37, 38]. With the participant of the SiO and CO, the temperature further dropped to some degree. During the ultra-precision machining process, the dynamic pressure always resulted in the formation of chemically active dangling bonds of both C and Si, which leads to the formation of SiC at much lower temperature (~450 ℃) in the cutting zone [35]. Therefore, the following chemical reaction has been proposed for the formation of SiC, SiO and SiO_2, and the negative free energy change make all of them possible in the grinding zone [20, 36].

$$\mathrm{Si(s,\ l,\ g)+C(s)\rightarrow SiC(s)},\quad \Delta G=-499.82+0.315T\ \mathrm{kJ/mol}$$

or

$$\mathrm{Si(s)+O_2(g)\rightarrow SiO_2(s)},\quad \Delta G=-670.4+0.327T\ \mathrm{kJ/mol}$$

$$\mathrm{SiO_2(s)+C(s)\rightarrow SiO(s)+CO(g)}$$

$$\mathrm{SiO(s)+3CO(g)\rightarrow SiC(s)+2CO_2(g)}$$

$$\mathrm{SiO(g)+C(s)\rightarrow Si(g)+CO(g)}$$

$$\mathrm{Si(g)+C(s)\rightarrow SiC(s)}$$

Moreover, the chemical reaction between Si and N, C and O can also be identified, where the formation of Si_3N_4 and graphite oxide (GO) is proposed under the high temperature. Both α- and β-Si_3N_4 are of hexagonal structure and Si is tetrahedrally coordinated. The formation of α-Si_3N_4 is favored at the temperature below the melting of Si while β-Si_3N_4 above the melting point [39]. At the high grinding temperature, the chemical reaction between the gaseous N_2 and solid Si took place, and two reaction mechanisms were proposed: the nitrogen firstly dissociates and then reacts with Si atoms or Si atoms reacts with the N_2 molecules directly [40]. For the formation of Si_3N_4, the Gibbs free energy can be estimated by the following equations [39],

$$3Si(s)+2N_2(g)\rightarrow Si_3N_4(s), \quad \Delta G = -723 + 0.315T \text{ kJ/mol}$$

$$3Si(l)+2N_2(g)\rightarrow Si_3N_4(s), \quad \Delta G = -874 + 0.405T \text{ kJ/mol}$$

In addition, the gaseous O_2 in air and the formation of SiO and SiO_2 both have influences on the formation of Si_3N_4, where the surface oxide layer prevents the further formation of Si_3N_4 on the machined Si surface, as indicated by the weak N1s intensity compared with the O1s peak in XPS result.

As shown in Fig. 5(c), the low peak intensity and area at 287.8 eV for the carbonyl C (C=O, 287.8 eV) indicates the appearance of GO [41]. There is no doubt that graphitization of the diamond could be induced under the high pressure [42], where the tetrahedrally bonded amorphous C or small graphite particle appeared under the dynamic pressure and high temperature [43]. For the small grain size of graphite, the oxidation can occur at temperatures ranging from 450 to 650 ℃ [44]. In addition, the

two separated peaks around 284.5 eV and 286.5 eV is also a good indication for the formation of graphite oxide [45, 46], and the chemical reaction is described as follows,

$$2xC(s)+yO_2(g)\rightarrow 2G_xO_y(s)$$

It has also been reported that the single crystalline Si (Si-I) firstly transformed to be the β-Sn structure (Si-II) which then turned to be amorphous Si under the rapid loading/unloading condition, but the Si-II structure converted to be R8 (Si-XII) and BC8 (Si-III) structure under slow unloading [13]. During the high spindle speed grinding process, the diamond grits distributed in the cylindrical surface of diamond wheel participated in the material removal, and the rapid loading and unloading process contributed to the formation of amorphous Si on the machined surface. The lower feed rate (4.17 μm per revolution) provides a slow loading/unloading condition for the generation of R8 (Si-XII) and BC8 (Si-III) phase. Especially after the wear of the sharp edge of the diamond wheel, the repeated loads make it more possible to form the metastable phases. Therefore, the R8 (Si-XII), BC8 (Si-III) and amorphous Si appeared on the machined surface. The transformation to be R8 (Si-XII) and BC8 (Si-III) structure can result in the 'pop-out' effect during the nano-indentation test [14]. During the single point diamond grinding process, the volume change accompanied by the phase transformation led to the generation of surface burs inevitably, as shown in Fig. 2(b). Due to the random protrusion height and distribution of the diamond grits, the loads and the surface burs also changed accordingly.

5. Conclusion

In the present study, the surface damage mechanism of monocrystalline Si during

single point diamond grinding (SPDG) was investigated based on the characterization by WLI, AFM, SEM, EDS, XRD, XPS and Raman spectroscopy. The results showed that the surface characteristics of the machined Si wafer differed at varied points of the grinding grooves due to the varied kinematics of the diamond grits in the cylindrical surface and end face of the wheel, where the surface formed by the cylindrical surface of the diamond wheel contributed to the ductile material removal while the diamond grits in the end surface caused the intermittent fracture. This also promoted the appearance of different Si allotropes for the varied loading/unloading condition of the diamond grits, and the phase transformation accompanied volume change resulted in the generation of surface burs. The scratching and friction effects, which led to the high grinding temperature, caused the chemical reaction between the Si, C, N_2 and O_2, and the formation of Si_3N_4 and graphite oxide (GO) is proposed as new surface damage mechanism and diamond tool wear mechanism based on the XPS results in the present work.

Acknowledgments

The work was partially supported by the National Natural Science Foundation of China (NSFC) (Project No.:51475109 and 51275231) and also the Research Committee of the Hong Kong Polytechnic University (RTRA).

References:

[1] J. Sun, L. Fang, J. Han, Y. Han, H. Chen, K. Sun, Phase transformations of mono-crystal silicon induced by two-body and three-body abrasion in nanoscale, Comp. Mater. Sci. 82 (2014) 140-150.

[2] W.J. Zong, T. Sun, D. Li, K. Cheng, Y.C. Liang, XPS analysis of the groove wearing marks on flank face of diamond tool in nanometric cutting of silicon wafer, Int. J. Mach. Tools Manuf. 48 (2008) 1678-1687.

[3] J. Yan, K. Syoji, J.I. Tamaki, Some observations on the wear of diamond tools in ultra-precision cutting of single-crystal silicon, Wear 255 (2003) 1380-1387.

[4] S. Gao, R. Kang, Z. Dong, B. Zhang, Edge chipping of silicon wafers in diamond grinding, Int. J. Mach. Tools Manuf. 64 (2013) 31-37.

[5] Q. Zhang, S. To, Q. Zhao, B. Guo, Recrystallization of amorphized Si during micro-grinding of RB-SiC/Si composites, Mater. Lett. 172 (2016) 48-51.

[6] Y. Wang, J. Zou, H. Huang, L. Zhou, B.L. Wang, Y.Q. Wu, Formation mechanism of nanocrystalline high-pressure phases in silicon during nanogrinding, Nanotechnology 18 (2007) 465705.

[7] J. Cheng, Y.D. Gong, Experimental study of surface generation and force modeling in micro-grinding of single crystal silicon considering crystallographic effects, Int. J. Mach. Tools Manuf. 77 (2014) 1-15.

[8] H. Li, T. Yu, L. Zhu, W. Wang, Analytical modeling of grinding-induced subsurface damage in monocrystalline silicon, Mater. Des. 130 (2017) 250-262.

[9] S. Gao, Z. Dong, R. Kang, B. Zhang, D. Guo, Warping of silicon wafers subjected to back-grinding process, Precis. Eng. 40 (2015) 87-93.

[10] A.S. Budiman, G. Illya, V. Handara, W.A. Caldwell, C. Bonelli, M. Kunz, N. Tamura, D. Verstraeten, Enabling thin silicon technologies for next generation c-Si solar PV renewable energy systems using synchrotron X-ray microdiffraction as

stress and crack mechanism probe, Sol. Energy Mater. Sol. Cells 130 (2014) 303-308.

[11] V.A. Handara, I. Radchenko, S.K. Tippabhotla, K.R. Narayanan, G. Illya, M. Kunz, N. Tamura, A.S. Budiman, Probing stress and fracture mechanism in encapsulated thin silicon solar cells by synchrotron X-ray microdiffraction, Sol. Energy Mater. Sol. Cells 162 (2017) 30-40.

[12] T.G. Bifano, T.A. Dow, R.O. Scattergood, Ductile-Regime Grinding: A New Technology for Machining Brittle Materials, J. Manuf. Sci. Eng. 113 (1991) 184-189.

[13] A. Kailer, Y.G. Gogotsi, K.G. Nickel, Phase transformations of silicon caused by contact loading, J. Appl. Phys. 81 (1997) 3057-3063.

[14] V. Domnich, Y. Gogotsi, S. Dub, Effect of phase transformations on the shape of the unloading curve in the nanoindentation of silicon, Appl. Phys. Lett. 76 (2000) 2214-2216.

[15] H. Huang, J. Yan, New insights into phase transformations in single crystal silicon by controlled cyclic nanoindentation, Scr. Mater. 102 (2015) 35-38.

[16] Z. Zhang, D. Guo, B. Wang, R. Kang, B. Zhang, A novel approach of high speed scratching on silicon wafers at nanoscale depths of cut, Sci. Rep. 5 (2015) 16395.

[17] B.V. Tanikella, A.H. Somasekhar, A.T. Sowers, R.J. Nemanich, R.O. Scattergood, Phase transformations during microcutting tests on silicon, Appl. Phys. Lett. 69 (1996) 2870-2872.

[18] L. Zhou, H. Eda, J. Shimizu, S. Kamiya, H. Iwase, S. Kimura, H. Sato, Defect-free

fabrication for single crystal silicon substrate by chemo-mechanical grinding, CIRP Ann. - Manuf. Technol. 55 (2006) 313-316.

[19] I. Zarudi, L.C. Zhang, Effect of ultraprecision grinding on the microstructural change in silicon monocrystals, J. Mater. Process. Technol. 84 (1998) 149-158.

[20] S. Goel, X. Luo, R.L. Reuben, Wear mechanism of diamond tools against single crystal silicon in single point diamond turning process, Tribol. Int. 57 (2013) 272-281.

[21] K.E. Puttick, L.C. Whitmore, P. Zhdan, A.E. Gee, C.L. Chao, Energy scaling transitions in machining of silicon by diamond, Tribol. Int. 28 (1995) 349-355.

[22] Y.E. Tohme, Grinding aspheric and freeform micro-optical molds, Proc. SPIE 6462 (2007) 64620K1-64620K8.

[23] Q. Zhang, Q. Zhao, S. To, B. Guo, A further study of wheel normal grinding of hemisphere couples on TiC-based cermet, Int. J. Adv. Manuf. Technol. 87 (2016) 2593-2602.

[24] F. Chen, S. Yin, H. Huang, H. Ohmori, Fabrication of small aspheric moulds using single point inclined axis grinding, Precis. Eng. 39 (2015) 107-115.

[25] H. Suzuki, M. Okada, Y. Yamagata, S. Morita, T. Higuchi, Precision grinding of structured ceramic molds by diamond wheel trued with alloy metal, CIRP Ann. - Manuf. Technol. 61 (2012) 283-286.

[26] T. Bletek, F. Klocke, M. Hünten, O. Dambon, Dressing of fine grained diamond grinding wheels for ultra precision grinding of structured molds in brittle hard materials, Optifab (2013) 888405-888408.

[27] E. Brinksmeier, Y. Mutlugünes, F. Klocke, J.C. Aurich, P. Shore, H. Ohmori, Ultra-precision grinding, CIRP Ann. - Manuf. Technol. 59 (2010) 652-671.

[28] Z. Hou, R. Komanduri, On the mechanics of the grinding process-Part I. Stochastic nature of the grinding process, Int. J. Mach. Tools Manuf. 43 (2003) 1579-1593.

[29] Q. Zhang, S. To, Q. Zhao, B. Guo, Surface generation mechanism of WC/Co and RB-SiC/Si composites under high spindle speed grinding (HSSG), Int. J. Refract. Met. Hard Mater. 56 (2016) 123-131.

[30] S. Malkin, C. Guo, Grinding technology: theory and applications of machining with abrasives, New York: Industrial Press, 2008.

[31] Q. Zhang, S. To, Q. Zhao, B. Guo, Surface damage mechanism of WC/Co and RB-SiC/Si composites under high spindle speed grinding (HSSG), Mater. Des. 92 (2016) 378-386.

[32] L. Ma, Y. Gong, X. Chen, Study on surface roughness model and surface forming mechanism of ceramics in quick point grinding, Int. J. Mach. Tools Manuf. 77 (2014) 82-92.

[33] Q. Zhao, B. Guo, Ultra-precision grinding of optical glasses using mono-layer nickel electroplated coarse-grained diamond wheels. Part 2: Investigation of profile and surface grinding, Precis. Eng. 39 (2015) 67-78.

[34] G. Spur, S.E. Holl, Ultrasonic assisted grinding of ceramics, J. Mater. Process. Technol. 62 (1996) 287-293.

[35] S. Goel, X. Luo, R.L. Reuben, H. Pen, Influence of temperature and crystal orientation on tool wear during single point diamond turning of silicon, Wear 284

(2012) 65-72.

[36] Z. Cheng, Reaction kinetics and structural evolution for the formation of nanocrystalline silicon carbide via carbothermal reduction, MSc Thesis-Materials Science and Engineering, Georgia Institute of Technology, 2004.

[37] Y. Zhang, T. Ichihashi, E. Landree, F. Nihey, S. Iijima, Heterostructures of single-walled carbon nanotubes and carbide nanorods, Science 285 (1999) 1719.

[38] X. Sun, C. Li, W. Wong, N. Wong, C. Lee, S. Lee, B. Teo, Formation of silicon carbide nanotubes and nanowires via reaction of silicon (from disproportionation of silicon monoxide) with carbon nanotubes, J. Am. Chem. Soc. 124 (2002) 14464-14471.

[39] A.J. Moulson, Reaction-bonded silicon nitride: its formation and properties, J. Mater. Sci. 14 (1979) 1017-1051.

[40] H.M. Jennings, On reactions between silicon and nitrogen, J. Mater. Sci. 18 (1983) 951-967.

[41] S. Stankovich, R.D. Piner, X. Chen, N. Wu, S.T. Nguyen, R.S. Ruoff, Stable aqueous dispersions of graphitic nanoplatelets via the reduction of exfoliated graphite oxide in the presence of poly (sodium 4-styrenesulfonate), J. Mater. Chem. 16 (2006) 155-158.

[42] Y.G. Gogotsi, A. Kailer, K.G. Nickel, Materials: transformation of diamond to graphite, Nat. 401 (1999) 663-664.

[43] Q. Zhang, Q. Zhao, H. Su, S. To, A systematic investigation on the diamond wear mechanism during the dry scratching of WC/Co, Int. J. Refract. Met. Hard Mater.

70 (2018) 184-190.

[44] J.R. Hahn, Kinetic study of graphite oxidation along two lattice directions, Carbon 43 (2005) 1506-1511.

[45] W. Gao, L.B. Alemany, L. Ci, P.M. Ajayan, New insights into the structure and reduction of graphite oxide, Nat. Chem. 1 (2009) 403-408.

[46] S. Park, J. An, J.R. Potts, A. Velamakanni, S. Murali, R.S. Ruoff, Hydrazine-reduction of graphite- and graphene oxide, Carbon 49 (2011) 3019-3023.